OU-HET-924, KEK-CP-356

Lattice calculation of vector and axial-vector current correlators in QCD

M. Tomii,[1,*] G. Cossu,[2] B. Fahy,[3] H. Fukaya,[4] S. Hashimoto,[3,5] T. Kaneko,[3,5] and J. Noaki[3]

(JLQCD Collaboration)

[1] *Physics Department, Columbia University, New York 10027, USA*

[2] *School of Physics and Astronomy, The University of Edinburgh, Edinburgh EH9 3JZ, United Kingdom*

[3] *Theory Center, Institute of Particle and Nuclear Studies, High Energy Accelerator Research Organization (KEK), Tsukuba 305-0801, Japan*

[4] *Department of Physics, Osaka University, Toyonaka 560-0043, Japan*

[5] *Department of Particle and Nuclear Physics, SOKENAI (The Graduate University for Advanced Studies), Tsukuba 305-0801, Japan*

arXiv:1703.06249v1 [hep-lat] 18 Mar 2017

Abstract

We study the vector and axial-vector current correlators in perturbative and non-perturbative regimes of QCD. The correlators are calculated on the lattice using the Möbius domain-wall fermion formulation at three lattice spacings covering 0.044–0.080 fm. The dynamical quark effects of 2+1 light flavors are included. The correlators calculated on the lattice after extrapolating to the physical point agree with those converted from the ALEPH experimental data of hadronic τ decays. We also extract the chiral condensate from the short-distance correlators on the lattice using the PCAC relation. Its result extrapolated to the chiral and continuum limit is compatible with other estimates at low energies.

* mt3164˙at˙columbia.edu

I. INTRODUCTION

Two-point current correlator is one of the most fundamental quantities in the study of Quantum Chromodynamics (QCD). It is defined as a vacuum expectation value of a product of quark currents, and reflects the QCD dynamics. It shows different aspects depending on the distance between the currents. At short distances (< 0.1 fm), it behaves perturbatively, *i.e.* the perturbative expansion about small coupling constant works reasonably well and several properties including its scaling are understood perturbatively. In this region, the effect of spontaneous chiral symmetry breaking is small and two correlators connected by the chiral transformation become almost degenerate. At long distances (> 1 fm), on the other hand, current correlators are saturated by the ground state and characterized by its mass and decay constant. The degeneracy among the chiral partners is clearly lost.

In the distance region between the two, ~ 0.1–1 fm, neither the perturbative nor the hadronic description is fully applicable. In the perturbative expansion, the terms of higher powers of the QCD coupling constant $\alpha_s(Q)$ become more significant, or the expansion even ceases to converge. This is related to the emergence of power corrections through $e^{1/\beta_0\alpha_s(Q)} \sim (\Lambda_{\rm QCD}/Q)$ due to the running of the coupling as a function of the scale Q, an inverse of the distance scale. The QCD scale $\Lambda_{\rm QCD}$ indeed characterizes the distance scale where the power corrections of the form $(\Lambda_{\rm QCD}/Q)^n$ become important. In the hadronic picture, this region is identified by many resonances and multi-body scattering states. The individual states involved are complicated, but the common belief is that the sum over a number of hadronic states can be interpreted as interacting quarks and gluons, *i.e.* quark-hadron duality. There are many evidences that this duality works, such as the perturbative description of the experimentally measured R ratio of the e^+e^- cross section, but theoretical understanding based on QCD is yet unsatisfactory.

Lattice QCD calculation is applicable to any distance scales in principle. So far, it has been successfully applied to calculate hadron correlators at long distances to extract hadron masses and matrix elements, and precise agreement with experimental data for many physical quantities is reported. In such calculation, the data at the short and middle distances are ignored to avoid "contaminations" from excited states, although they may contain the interesting information about the intermediate regime where the quark and hadron pictures overlap. In this work, we explore this regime using lattice data.

The vector and axial-vector current correlators may be related to hadronic τ decays and e^+e^- hadronic cross section through the optical theorem, which involves a weighted integral over momentum transfer squared. This connection between the correlators and experimental data allows us to compare the lattice calculation with experiments in the region where excited states contribute significantly.

The vector and axial-vector current correlators were reconstructed using the early experimental data [1, 2]. It provides the correlators in the coordinate space with space-like separation x between the currents. It is equivalent to the space-like correlators in the momentum space after an appropriate Fourier transform, but allows more direct comparison with the lattice calculation. In the past, such comparison was attempted using quenched simulations [3–5]. With considerable progress of lattice calculation and updated experimental data after these works, we revisit the problem.

In this work, we study the correlators of the iso-triplet vector and axial-vector currents. The most recent experimental data for these correlators are obtained through the hadronic τ decay experiment by the ALEPH collaboration [6]. The experiment provides the spectral functions as a function of the invariant mass s, whose kinematical upper limit is set by the τ lepton mass m_τ^2. The spectral function above this limit needs to be estimated using perturbation theory, which is available to the order of α_s^4 [7, 8] and reliable at sufficiently large invariant masses. At lower invariant masses, the observed spectral functions show significant deviation from the perturbative prediction due to a violation of the quark-hadron duality [9–12]. The duality violation may be modeled using the Regge theory with large-N_c assumption [11–14].

Our lattice calculation is performed on the gauge ensembles of 2+1-flavor QCD. We employ the Möbius domain-wall fermion formulation [15, 16] for both sea and valence quarks. Since the discretization effect may become more significant in the distance scales below 1 fm than in the hadron mass measurements from long-distance correlators, we take the continuum limit using the ensembles with lattice spacing $a \simeq 0.080$, 0.055 and 0.044 fm. As a result, the correlators in the distances longer than $\simeq 0.4$ fm are obtained with errors well under control. The same set of gauge ensembles has been used for the studies of heavy-light decay constant [17] and D meson semileptonic form factors [18], the determination of charm quark mass [19], and a calculation of the chiral condensate [20] and η' mass [21].

We use the local vector and axial-vector currents constructed with the Möbius domain-

wall fermion. Since these currents are not conserving, a finite renormalization is needed. In our previous work [22], we determined the renormalization factor using the correlators in the perturbative regime based on the X-space renormalization procedure [23–25]. Namely, we determine the renormalization factor such that the lattice correlators at short distances reproduce the continuum perturbative calculation available up to the order of α_s^4 [26]. Since the chiral symmetry on the lattice is precisely maintained, the renormalization factors of the vector and axial-vector currents are identical. The present work is a natural extension of the previous one, as the deviation from the perturbative regime is the main concern.

Besides the comparison with the experiments, we extract the chiral condensate from the vector and axial-vector correlators. It appears as the leading power correction to the correlators reflecting the spontaneous chiral symmetry breaking in QCD. The extraction is done based on the PCAC relation, with which the derivative of the axial-vector correlator is directly related to the chiral condensate [27]. With a good control of the discretization effect, we are able to determine the chiral condensate and the result is consistent with another determination from the spectral density of the Dirac operator [20].

This paper is organized as follows. In Section II, we discuss the vector and axial-vector current correlators in the continuum theory including the conversion of the experimental data through the dispersion relation. The relation between the chiral condensate and the axial-vector correlator is also discussed. In Section III, we summarize our lattice setup and describe the method to reduce the discretization effect in the lattice correlators. The comparison of the lattice data with the experiment and the extraction of the chiral condensate are shown in Section IV. Section V concludes the paper with some discussions.

II. CURRENT CORRELATORS

In this work, we study the two-point correlation functions of the iso-triplet vector and axial-vector currents in the Euclidean coordinate space,

$$\Pi_{V,\mu\nu}(x) = \langle V_\mu(x) V_\nu(0)^\dagger \rangle, \qquad \Pi_{A,\mu\nu}(x) = \langle A_\mu(x) A_\nu(0)^\dagger \rangle, \tag{1}$$

where the currents are defined by

$$V_\mu(x) = \bar{u}(x)\gamma_\mu d(x), \qquad A_\mu(x) = \bar{u}(x)\gamma_\mu\gamma_5 d(x), \tag{2}$$

with up and down quark fields $u(x)$ and $d(x)$. We also analyze the sum of the Lorentz diagonal components,

$$\Pi_{V/A}(x) = \sum_{\mu} \Pi_{V/A,\mu\mu}(x). \tag{3}$$

In this work, we assume the masses of up and down quarks are degenerate.

In the momentum space, the corresponding vacuum polarization tensors $\widetilde{\Pi}_{V/A,\mu\nu}(Q)$ are given by

$$\begin{aligned}\widetilde{\Pi}_{V/A,\mu\nu}(Q) &= \int \mathrm{d}^4x \ \mathrm{e}^{-\mathrm{i}Qx} \ \Pi_{V/A,\mu\nu}(x) \\ &= (Q^2\delta_{\mu\nu} - Q_\mu Q_\nu)\widetilde{\Pi}^{(1)}_{V/A}(q^2) - Q_\mu Q_\nu \widetilde{\Pi}^{(0)}_{V/A}(q^2),\end{aligned} \tag{4}$$

where $\widetilde{\Pi}^{(J)}_{V/A}(q^2)$ stands for the vacuum polarization function in the spin J channel written as a function of the momentum squared in the Minkowski space $q^2 = -Q^2$.

A. Correlators from experiment

The vector and axial-vector correlators $\Pi_{V/A}(x)$ in the coordinate space are related to the experimental observables through the dispersion relation. In the momentum space, it is given by the well-known analyticity formula

$$\widetilde{\Pi}^{(J)}_{V/A}(q^2) = \frac{1}{\pi}\int_0^\infty \mathrm{d}s \frac{\mathrm{Im}\ \widetilde{\Pi}^{(J)}_{V/A}(s)}{s - q^2} - \text{subtraction}. \tag{5}$$

Inserting this to (4) and applying the Fourier transform back to the coordinate space, the correlators are found to be [1, 2]

$$\Pi_{V/A}(x) = \frac{1}{8\pi^4}\int_0^\infty \mathrm{d}s \ s^{3/2}\left(3\rho^{(1)}_{V/A}(s) - \rho^{(0)}_{V/A}(s)\right)\frac{K_1(\sqrt{s}|x|)}{|x|}, \tag{6}$$

where K_1 is the modified Bessel function and $\rho^{(J)}_{V/A}(s) = 2\pi\ \mathrm{Im}\ \widetilde{\Pi}^{(J)}_{V/A}(s)$ is the *so-called* spectral function. The second term on the RHS of (5), an unphysical contact term, is proportional to $\delta(|x|)$ in the coordinate space and therefore omitted from (6) and in the following discussions.

The spectral function represents the hadronic spectrum associated with the corresponding current and spin J. The spin-1 part $\rho^{(1)}_{V/A}(s)$ is measured by the hadronic τ decay experiments [6, 28–30]. The spin-0 part of the vector channel vanishes in the isospin limit, while that of

the axial-vector channel is dominated by the pion pole, $\rho_A^{(0)}(s) \propto f_\pi^2 \delta(s - m_\pi^2)$ with m_π and f_π being the pion mass and the decay constant, respectively.

Schäfer and Shuryak [2] converted $\rho_{V/A}^{(1)}(s)$ measured by ALEPH [28, 29] to the correlators (6), while the contribution of the spin-0 part $\rho_A^{(0)}(s)$ of the axial-vector channel is approximated by using the mass and the decay constant of the pion as explained above. Their result was used for a test of the consistency with a quenched lattice simulation [5].

In this work, we use the latest ALEPH data for $\rho_{V/A}^{(1)}(s)$ from the τ decay experiment [6] to calculate

$$\Pi_{V/A}^{(1)}(x) = \frac{3}{8\pi^4} \int_0^\infty \mathrm{d}s \; s^{3/2} \rho_{V/A}^{(1)}(s) \frac{K_1(\sqrt{s}|x|)}{|x|}, \tag{7}$$

which does not contain the contribution of the spin-0 part. In Section IV A–IV B, we show the result of the lattice calculation for $\Pi_{V/A}^{(1)}(x)$ extrapolated to the physical point and discuss the consistency with the experiment.

Since the spectral functions obtained from hadronic τ decays are measured in a limited region of the invariant mass lower than the τ lepton mass, $s < m_\tau^2$, we need to complement using some theory or model for the region $s > m_\tau^2$ in order to estimate the integral in (7). The spectral functions in perturbation theory are calculated to order α_s^4 [7, 8], which allows us to precisely estimate the spectral functions in the perturbative regime. Another possibility is to use the Operator Product Expansion (OPE) technique [31], but it is known that the OPE of the spectral functions in the Minkowski domain disagrees with that in full QCD beyond the uncertainty due to the truncation of the perturbative expansion and the operator expansion [9–12]. (Such disagreement is usually referred to as the quark-hadron duality violation.) Due to this, one needs to rely on models to estimate the spectral functions in the region beyond the experimental reach. Following a widely used model based on the Regge theory with the large-N_c assumption [11–14], we parametrize the spectral functions at large s as

$$\rho_{V/A}^{(1)}(s) = \rho_{V/A}^{\mathrm{pert}}(s) + \mathrm{e}^{-\delta_{V/A} - \gamma_{V/A} s} \sin\left(\alpha_{V/A} + \beta_{V/A} s\right), \tag{8}$$

with the perturbative part $\rho_{V/A}^{\mathrm{pert}}(s)$ of the spectral functions [7, 8] and unknown parameters $\delta_{V/A}$, $\gamma_{V/A}$, $\alpha_{V/A}$ and $\beta_{V/A}$. The remnant of resonances appears as the oscillatory term with exponential suppression at higher energies.

We perform a global fit for the vector and axial-vector spectral functions measured by ALEPH [6] to determine the unknown parameters $\delta_{V/A}$, $\gamma_{V/A}$, $\alpha_{V/A}$ and $\beta_{V/A}$ taking account

of the correlation between these two channels. We choose the fit range 1.6 $\mathrm{GeV}^2 \leq s \leq$ 2.7 GeV^2, in which the fit function (8) is supposed to be valid and the statistical uncertainty of the experimental data is not too large. As a result of the global fit, we obtain the parameters as

$$\begin{aligned} &\delta_V = 0.32(27), \quad \gamma_V = 0.72(9)\ \mathrm{GeV}^{-2}, \quad \alpha_V = -2.4(9), \quad \beta_V = 4.3(2)\ \mathrm{GeV}^{-2}, \\ &\delta_A = -1.5(5), \quad \gamma_A = 1.7(2)\ \mathrm{GeV}^{-2}, \quad \alpha_A = 2.2(4.8), \quad \beta_A = 3.6(1.2)\ \mathrm{GeV}^{-2}. \end{aligned} \tag{9}$$

The χ^2 divided by the degrees of freedom is 1.3.

Figure 1 shows the spectral functions in the vector (upper panel) and axial-vector (lower panel) channels measured by ALEPH [6]. The dotted and solid lines stand for the prediction of the parton model (corresponding to the leading order perturbation theory) and the perturbation theory at $O(\alpha_s^4)$, respectively. The fit result is represented by the dashed curve and the band. For the vector channel, the effect of the duality violation is visible as a bump around $s \simeq 2.5\ \mathrm{GeV}^2$. In order to converge towards the perturbative prediction at high energies, the oscillatory and decaying function of the form $\mathrm{e}^{-\delta_{V/A}-\gamma_{V/A}s}\sin(\alpha_{V/A}+\beta_{V/A}s)$ is necessary.

The correlators reconstructed through (7) are shown in Figure 2. They are normalized by the tree-level value $R_{V/A}(x) = \Pi^{(1)}_{V/A}(x)/\Pi_0(x)$ with $\Pi_0(x)$ being the correlator in the massless free theory, which is common for both vector and axial-vector channels. We divide the integral (7) into two regions at $s_0 = 2.7\ \mathrm{GeV}^2$. Below s_0, we directly input the spectral functions from the experiment, while the spectral functions of the massless perturbation theory with (solid band) and without (hatched band) the duality-violating term are used above s_0. There are two remaining experimental data for each channel above s_0 discarded in this analysis due to the large statistical errors. At short distances (< 0.2 fm), these correlators agree with the prediction of massless perturbation theory (dotted line) [26].

One can see that the impact of the duality-violating term is not very significant. This is reasonable because the effect of the duality violation is smeared out by the dispersion integral. The vacuum polarization function in the space-like region is insensitive to the individual poles in the Minkowski domain. We show the consistency between these results with lattice calculation in Section IV A–IV B.

It is convenient for later discussions to investigate the amount of non-perturbative contributions to the correlators at each distance $|x|$. Figure 3 shows the decomposition of $R_V(x)$

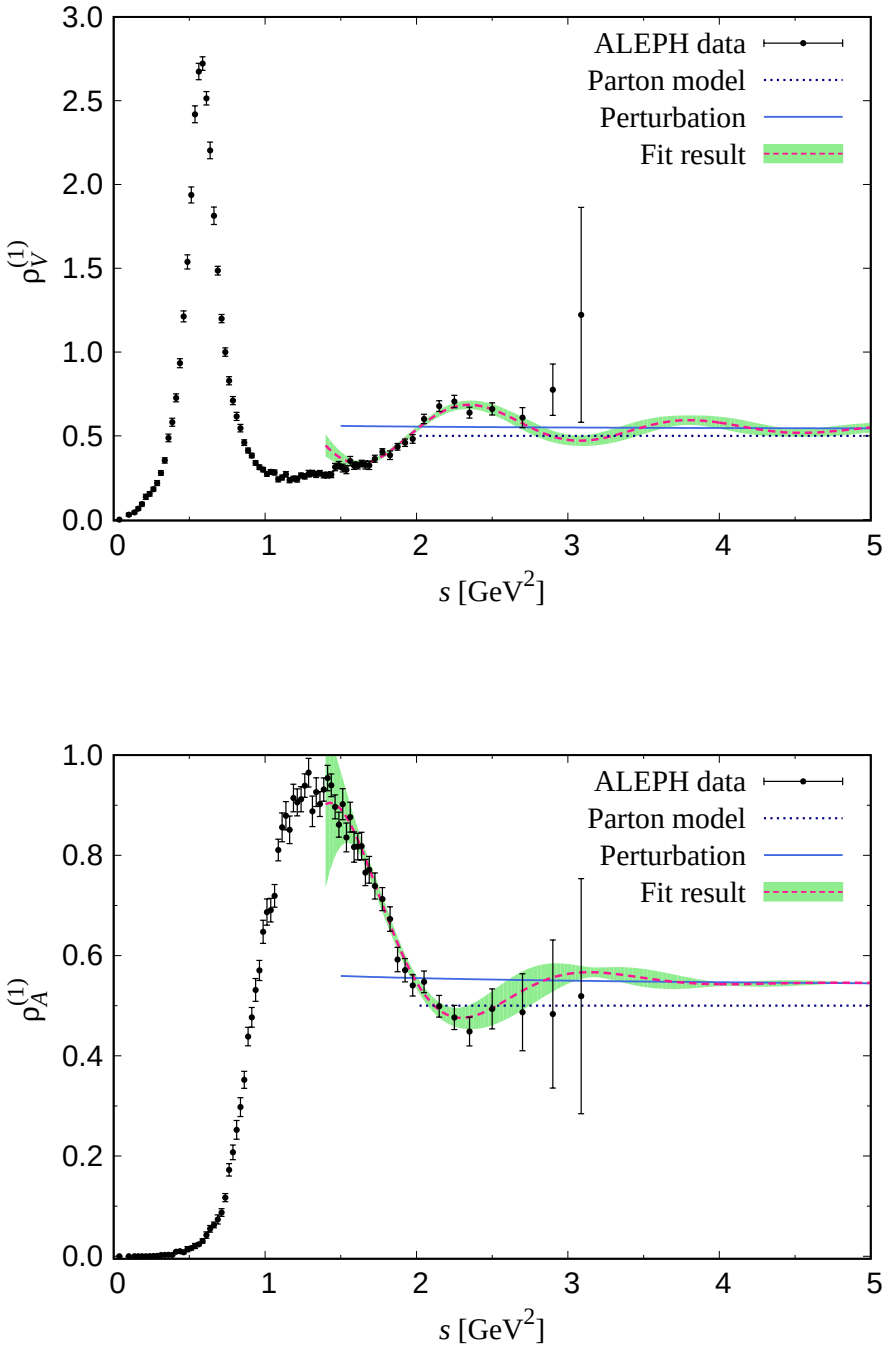

FIG. 1. Spectral functions of the vector (upper) and axial-vector (lower) channels measured by the ALEPH collaboration (circles) [6] as functions of s. The prediction of the parton model (dotted line), perturbation theory (solid line) and the fit result (dashed curve and band) using the fit function (8) are also shown.

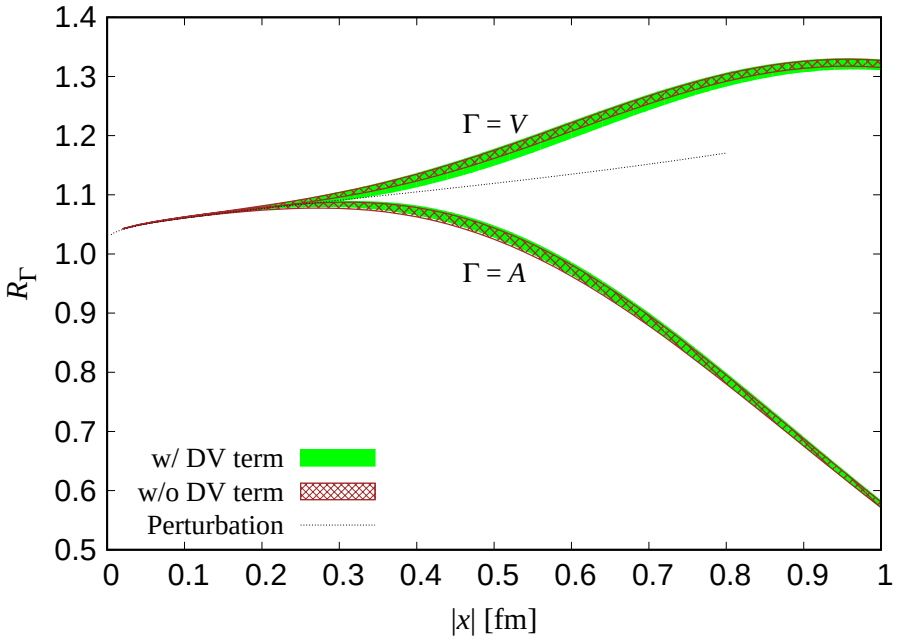

FIG. 2. Vector and axial-vector correlators reproduced using the dispersion relation (7). The spectral functions measured by ALEPH are used for $s \leq 2.7$ GeV^2, while those in $s > 2.7$ GeV^2 are calculated perturbatively with (solid band) and without (hatched band) the duality-violating term. The prediction of the massless perturbation theory is also shown (dotted line).

into the contributions of the spectral function in different regions of s. The area indicated by "Perturbation" represents the contribution of the spectral function in $s > 2.7$ GeV^2, which is calculated perturbatively. For more non-perturbative regime, we split the region $s \leq 2.7$ GeV^2 into the ρ meson resonance $(0.776-0.150)^2$ GeV$^2 < s < (0.776+0.150)^2$ GeV^2, plus above and below it. We also show the corresponding plot for the axial-vector channel in Figure 4. The region of s indicated by "Perturbation" is the same as for the vector channel $s > 2.7$ GeV^2, while the resonance of the a_1 meson is chosen as $(1.23 - 0.40)^2$ GeV$^2 < s < (1.23 + 0.40)^2$ GeV^2. Both plots indicate that the non-perturbative effect is quite significant in the distance region around $|x| \simeq 0.5$ fm, but the correlators are not saturated by the ground state. This is the region that we are interested in, *i.e.* both perturbative expansion and low-energy effective theories are not fully applicable. In Section IV A–IV B, we demonstrate that the lattice calculation succeeds to reproduce the experimental results at $|x| \simeq 0.5$ fm.

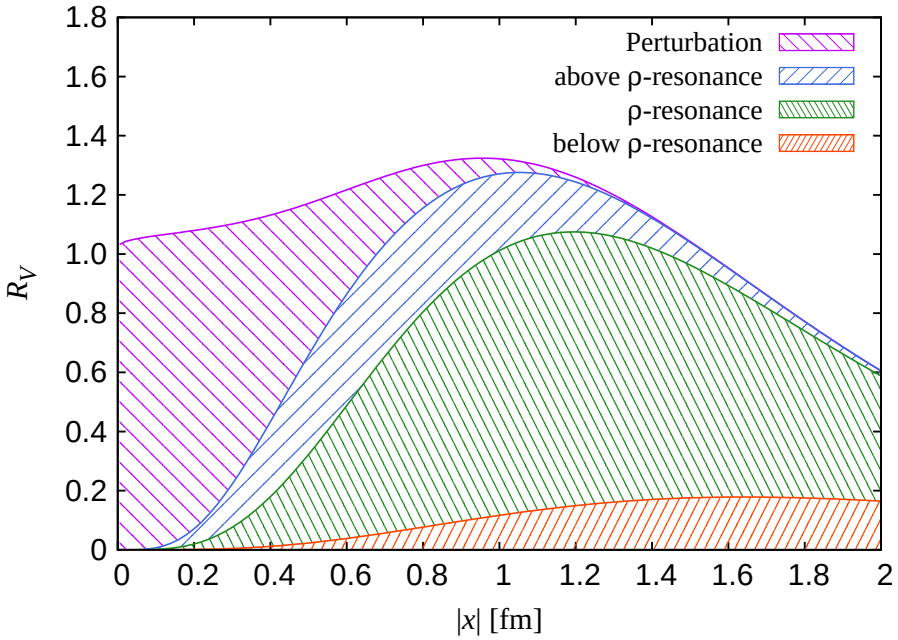

FIG. 3. Decomposition of the vector correlators into the contributions from the spectral function in different regions of s.

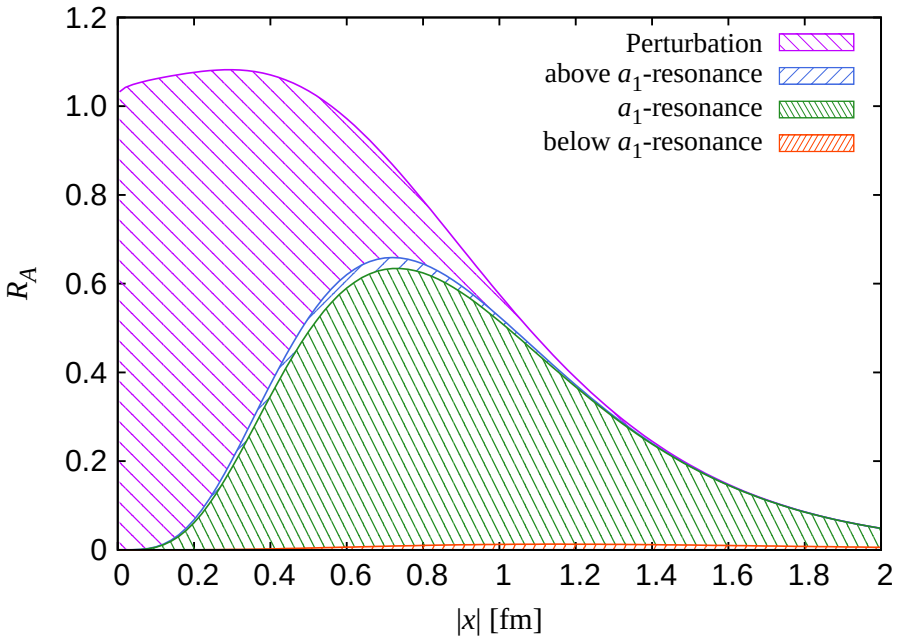

FIG. 4. Same as Figure 4 but for the axial-vector channel.

B. Chiral condensate through PCAC relation

While the spin-1 part of the vector and axial-vector correlators is related to the hadronic τ decays as discussed in the previous subsection, their spin-0 part is sensitive to another feature of QCD. In the isospin limit, the spin-0 part of the vector channel vanishes, and only the axial-vector channel is non-trivial.

According to the PCAC relation, projection of the axial-vector correlator to the spin-0 part is achieved by taking its divergence. Using the PCAC relation, we can relate the axial-vector correlator to the chiral condensate $\langle\bar{q}q\rangle$ as follows. The spin-0 part of the axial-vector correlator is given by [27, 32]

$$\widetilde{\Pi}_A^{(0)}(q^2) = \frac{4m_q}{q^4}\langle\bar{q}q\rangle + \frac{4m_q^2}{q^4}\widetilde{\Pi}_P(q^2), \tag{10}$$

where m_q is the degenerate mass of up and down quarks and

$$\widetilde{\Pi}_P(q^2) = \int \mathrm{d}^4x\ \mathrm{e}^{-\mathrm{i}Qx}\langle\bar{u}\mathrm{i}\gamma_5 d(x)\cdot\bar{d}\mathrm{i}\gamma_5 u(0)\rangle. \tag{11}$$

Therefore, the Fourier transform of (4) leads to

$$-\frac{\pi^2}{2m_q}x^2\sum_{\mu,\nu}x_\nu\partial_\mu\Pi_{A,\mu\nu}(x) = -\langle\bar{q}q\rangle + O(m_q). \tag{12}$$

Here, the renormalization scheme and scale dependence of m_q account for those of $\langle\bar{q}q\rangle$. Taking the chiral limit of (12), we can extract the chiral condensate $\Sigma = -\lim_{m_q\to 0}\langle\bar{q}q\rangle$. In Section IV C, we calculate the chiral condensate based on this relation.

III. LATTICE CALCULATION

In this work, we use the lattice ensembles generated with $2+1$-flavor dynamical Möbius domain-wall fermions [15, 16]. The tree-level improved Symanzik action [33] is used for the gauge part and the fermions couple to the gauge link after three steps of the stout smearing [34]. The gauge ensembles used in this analysis are summarized in Table I.

The lattice spacing a ranges between 0.044 and 0.080 fm, with which we take the continuum limit. Its value is determined through the Wilson-flow scale $t_0^{1/2}$ [35] with an input $t_0^{1/2}$ = 0.1465(21)(13) fm taken from [36]. Degenerate up and down quark masses m_q cover the range of corresponding pion mass between 230 and 500 MeV. They are used for both sea

TABLE I. Lattice ensembles used in this work.

β	a [fm]	$N_s^3 \times N_t \times L_s$	am_s	am_q	am_{res}	aM_π	$N_{\rm conf}$	$N_{\rm src}$
4.17	0.0804	$32^3 \times 64 \times 12$	0.0300	0.0070	0.00017(1)	0.1263(4)	200	4
				0.0120	0.00015(2)	0.1618(3)	200	2
				0.0190	0.00015(3)	0.2030(3)	200	2
		$48^3 \times 96 \times 12$	0.0400	0.0035	0.00022(2)	0.0921(1)	200	2
		$32^3 \times 64 \times 12$		0.0070	0.00023(4)	0.1260(4)	200	4
				0.0120	0.00012(8)	0.1627(3)	200	2
				0.0190	0.00015(3)	0.2033(3)	200	2
4.35	0.0547	$48^3 \times 96 \times 8$	0.0180	0.0042	$\sim 10^{-5}$	0.0820(3)	200	2
				0.0080		0.1127(3)	200	1
				0.0120		0.1381(3)	200	1
			0.0250	0.0042		0.0831(4)	200	2
				0.0080		0.1130(3)	200	1
				0.0120		0.1387(3)	200	1
4.47	0.0439	$64^3 \times 128 \times 8$	0.0150	0.0030		0.0632(2)	200	1

and valence quarks. Strange quark is, on the other hand, only in the sea, and its mass m_s is taken close to the physical value. The residual mass m_{res} is $O(1)$ MeV on the coarsest lattice and much smaller than that on finer lattices. For each ensemble, $N_{\rm conf} = 200$ configurations are sampled from 5,000 molecular dynamics time. On each configuration, we calculate the correlators with one or more ($N_{\rm src}$) source points. We use the IroIro++ simulation code [37] for these calculations.

We calculate the current-current correlators $\Pi_{V/A,\mu\nu}(x)$ in (1) with the local vector and axial-vector currents defined on the lattice with the Möbius domain-wall fermion. We average the correlators over the lattice points that are related by 90° rotations. In this way the lattice points of different orientations are distinguished even when they have the same x^2. Namely, the points equivalent to the coordinate (1,1,1,1) are distinguished from those to (2,0,0,0), since they receive different discretization effects.

As discussed in the previous paper [22], we apply some cuts and corrections to reduce the

discretization effects. First, we subtract the dominant discretization effect by subtracting the correlators constructed from lattice quarks and add back their continuum counterparts. This procedure is further improved by using the mean-field approximation instead of the free propagator [38]. In addition, we discard the data points that are expected to have large remaining discretization effects. The criterion for the cut is given by an angle θ between the position vector x and the direction (1,1,1,1). Since the lattice data at large θ tend to have large discretization effects [3, 25], we neglect the lattice data of $\theta \geq 30°$. This particular value is chosen such that the points with a same x^2 become consistent within the statistical error. More details are described in [22].

IV. RESULT

A. Consistency of the lattice data with ALEPH in the $V + A$ channel

In this subsection, we discuss the consistency between the correlators calculated on the lattice and those converted from the ALEPH data for hadronic τ decays. The conversion of the experimental data is discussed in Section II A. Here, we analyze the sum and difference of the vector and axial-vector correlators, *i.e.* the $V + A$ and $V - A$ channels, normalized by the corresponding free correlator $\Pi_0(x)$ in the massless limit

$$R_{V\pm A}(x) = \frac{\Pi_V^{(1)}(x) \pm \Pi_A^{(1)}(x)}{2\Pi_0(x)}. \tag{13}$$

For the lattice calculation, the vector and axial-vector currents need to be renormalized since the local currents we use in this work are not conserving. The renormalization is done multiplicatively, *i.e.* $R_{V\pm A}(x) \to Z_V^{\overline{\rm MS}}(a)^2 R_{V\pm A}(x)$, with $Z_V^{\overline{\rm MS}}(a)$ being the renormalization factor of the vector and axial-vector currents determined in the previous work [22].

Since the quantities $R_{V\pm A}(x)$ do not contain the spin-0 contribution, we need to subtract the spin-0 part from the lattice correlators as well to obtain the spin-1 piece $\Pi_{V/A}^{(1)}(x) = \Pi_{V/A}(x) - \Pi_{V/A}^{(0)}(x)$. For the vector channel, the spin-0 part is absent in the isospin limit, $\Pi_V^{(0)}(x) = 0$. For the axial-vector channel, we approximate the spin-0 part $\Pi_A^{(0)}(x)$ by the contribution of the ground state pion. In the infinite volume, it is given by

$$\Pi_A^{(0),\infty}(x) \simeq \frac{z_0 M_\pi^2}{2\pi^2} \frac{K_1(M_\pi|x|)}{|x|}, \tag{14}$$

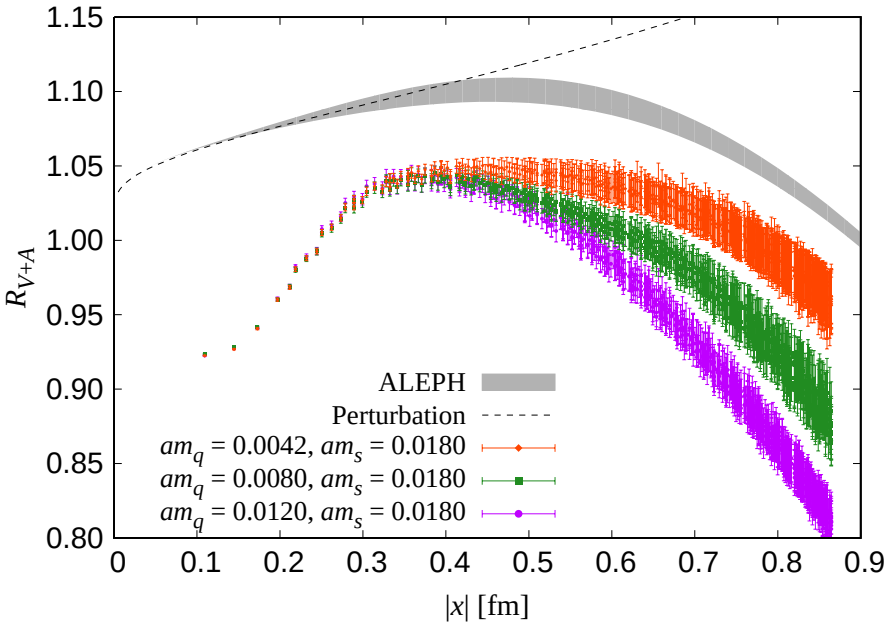

FIG. 5. R_{V+A} calculated on the ensembles at $\beta = 4.35$, $am_s = 0.0180$ and three input light quark masses $am_q = 0.0042$ (diamonds), 0.080 (squares) and 0.0120 (circles). The prediction of massless perturbation theory (dashed curve), the results of the experiments calculated with the duality-violating term in (8) (band) are also shown.

where z_0 and M_π are extracted from the zero-momentum correlator $\int \mathrm{d}^3x\ \Pi_{A,44}(\vec{x},t) \to z_0 \mathrm{e}^{-M_\pi t}$ at large time separations. We neglect the excited states of the pion because they are not expected to give significant contributions. In a finite box, the finite volume effect due to the pion pole may appear. To take account of this, we subtract the wrap-around effect of the pion and analyze

$$\Pi_A^{(1)}(x) = \Pi_A(x) - \sum_{x_0} \Pi_A^{(0),\infty}(x - x_0), \tag{15}$$

where the sum over x_0 runs over

$$x_0 \in \{(0,0,0,0), (\pm L,0,0,0), (0,\pm L,0,0), (0,0,\pm L,0), (0,0,0,\pm T), (\pm L,\pm L,0,0), \ldots\}. \tag{16}$$

Figure 5 shows the results for $R_{V+A}(x)$ on the ensembles at $\beta = 4.35$, $am_s = 0.0180$ with different light quark masses, $am_q = 0.042$, 0.080 and 0.0120. Here, we also show the prediction of massless perturbation theory [26] (dashed line) and the experimental result (band) from the dispersion relation, where the spectral functions $\rho_{V/A}(s)$ in $s > 2.7$ GeV^2

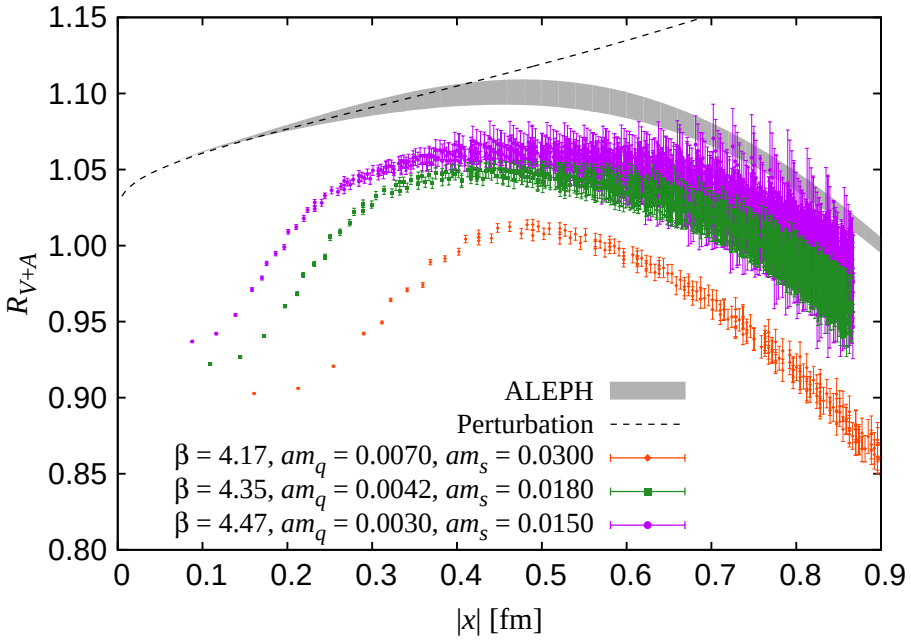

FIG. 6. Same as Figure 5 but calculated on the ensembles at different lattice cutoffs and a matched pion mass $M_\pi \simeq 300$ MeV.

include the duality-violating term in (8). In Figure 5, one can see that the results at smaller masses are closer to the experimental result.

Figure 6 shows the results at a matched pion mass $M_\pi \simeq 300$ MeV but at different β's. We find a significant dependence on the lattice spacing, which can be described by the leading term $\propto a^2$ at middle and long distances. As we approach the continuum limit, the lattice data tend to approach the experimental data.

We extrapolate these lattice results to the physical point, *i.e.* the continuum limit $a \to 0$ and physical pion mass $m_\pi \simeq 140$ MeV. To do so, we first divide the range of $|x|$ into N bins,

$$B_i = [x_i - \delta x/2, x_i + \delta x/2], \quad x_{i+1} = x_i + \delta x, \quad i = 1, 2, \ldots, N, \tag{17}$$

where x_i and δx are the center of the ith bin and the width of bins, respectively. For each bin, we average $R_{V+A}(x)$ over lattice points x in B_i. Since the average depends on the lattice spacing, input mass and the representative distance x_i of the correlator, the average is denoted by $\overline{R}_{V+A}(a, M_\pi, x_i)$ with the explicit dependence on these parameters. Here, we neglect the dependence on the strange quark mass because we do not find significant

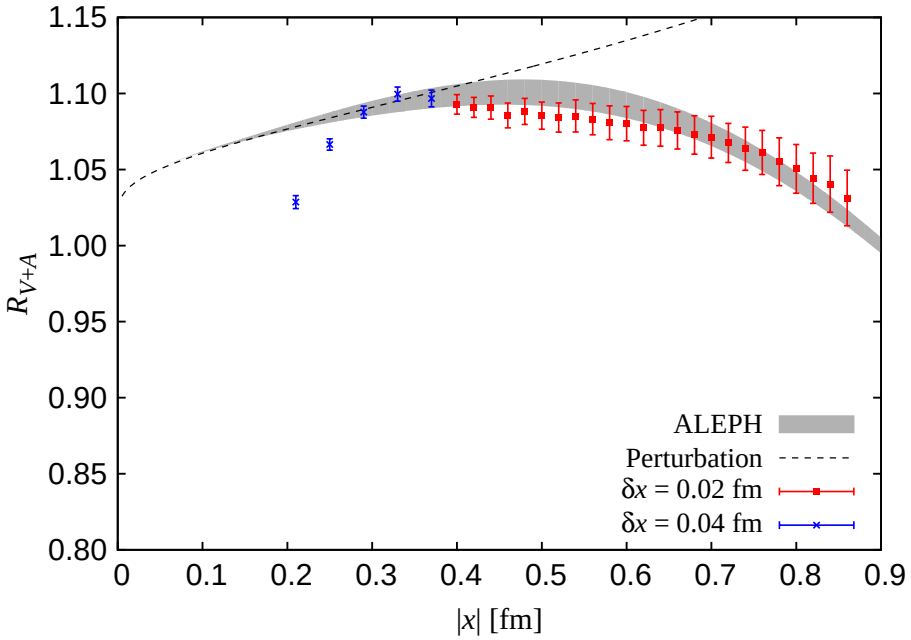

FIG. 7. Lattice result for R_{V+A} after the chiral and continuum extrapolations. Data in each bin are extrapolated assuming (18). Bin size is larger in the short-distance region $|x| \lesssim 0.4$ fm (blue crosses) than others (red squares) as the number of lattice points are fewer.

dependence in the lattice results. We then perform a global fit for all ensembles using the fit function

$$\overline{R}_{V+A}(a, M_\pi, x_i) = R_{V+A}(0, m_\pi, x_i) + c_i(M_\pi^2 - m_\pi^2) + d_i a^2, \tag{18}$$

with three free parameters $R_{V+A}(0, m_\pi, x_i), c_i$ and d_i for each i. The first parameter $R_{V+A}(0, m_\pi, x_i)$ corresponds to the extrapolated value. The other parameters c_i and d_i are to control the dependences on the pion mass and the lattice spacing, respectively.

Figure 7 shows the result of the extrapolation. Here, we take $\delta x = 0.02$ fm for $x_i \geq 0.4$ fm and $\delta x = 0.04$ fm for $x_i < 0.4$ fm. While the agreement between the lattice result and the experiment is found for $|x| > 0.3$ fm in the plot, the fit function (18) may not be appropriate at short distances due to remnant discretization effect that could not be removed by the extrapolation linear in a^2. In order to clarify the appropriate region of the fit function, we show the fit result of the coefficient d_i in Figure 8 and χ^2/dof in Figure 9. In Figure 8, the coefficient d_i varies quite rapidly at $|x| \simeq 0.4$ fm, while it is mostly constant at longer distances. As Figure 9 shows, χ^2/dof in $|x| < 0.4$ fm is much larger than that in the longer distance regime. These results imply that the remnant discretization effect of order $O(a^4)$

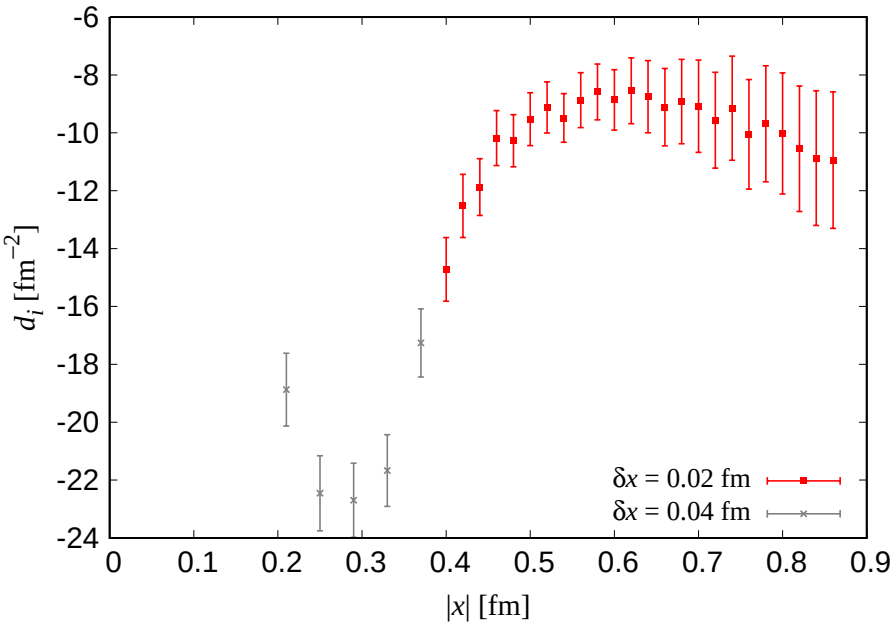

FIG. 8. Fit parameter d_i obtained from the extrapolation of $R_{V+A}(x)$ to the physical point. The result for each bin is plotted as a function of $|x| = x_i$.

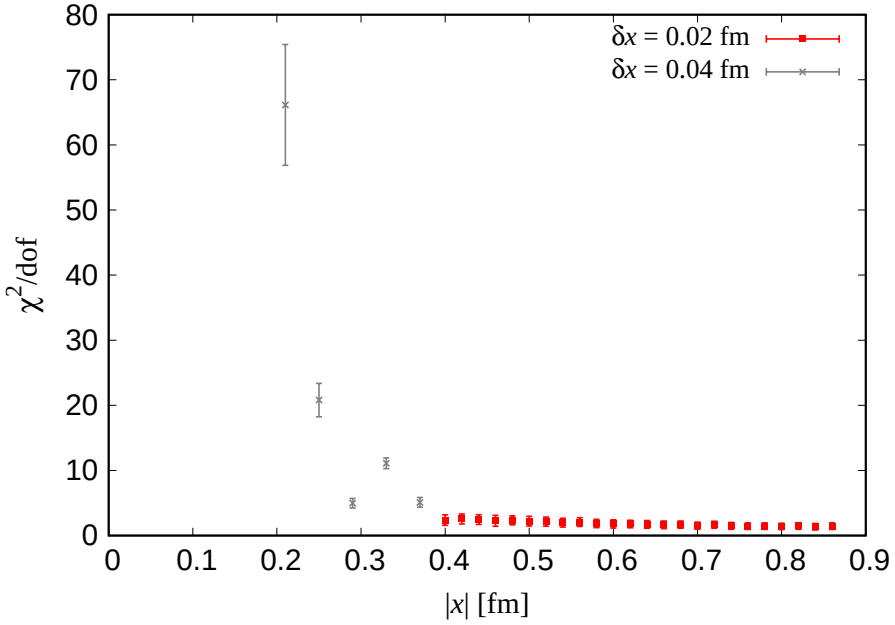

FIG. 9. χ^2 divided by the degrees of freedom for the extrapolation of $R_{V+A}(x)$ to the physical point. The result for each bin is plotted as a function of $|x| = x_i$.

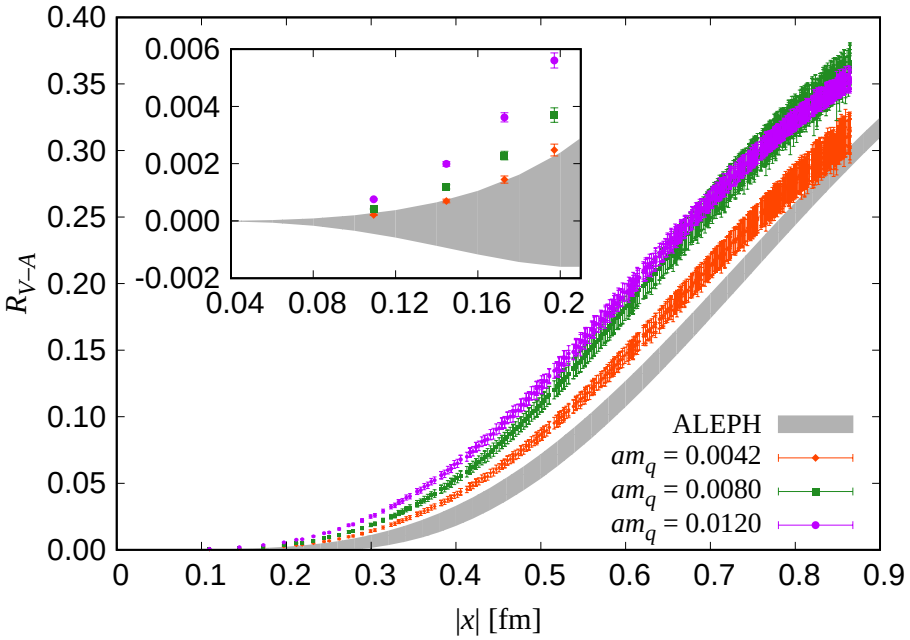

FIG. 10. R_{V-A} calculated on the ensembles at $\beta = 4.35$, $am_s = 0.0180$ and three input light quark masses $am_q = 0.0042$ (diamonds), 0.080 (squares) and 0.0120 (circles). The results from the experiments converted including the duality-violating term in (8) (band) are also shown.

is not negligible in $|x| < 0.4$ fm.

We may conclude that the lattice QCD calculation successfully reproduces the spectral function observed in the experiment in the length scale of 0.4 fm and longer. The agreement around $|x| \sim 0.5$ fm is important since the precise calculation of the correlators in this region is difficult with the perturbative approaches and with the low-energy effective theories as discussed in Section II A.

B. Consistency of the lattice data with ALEPH in the $V - A$ channel

Next, we report the results for $R_{V-A}(x)$. Figure 10 shows the lattice data at three different input masses at the same lattice spacing, $\beta = 4.35$. As expected, $R_{V-A}(x)$ vanishes in the short-distance limit because of the good chiral symmetry of the Möbius domain-wall fermion. At short distances ($\lesssim 0.5$ fm), the dependence on the input mass is clearly seen and the results at smaller masses are closer to the experimental result.

In Figure 11, which shows the results at the matched pion mass $M_\pi \simeq 300$ MeV and at

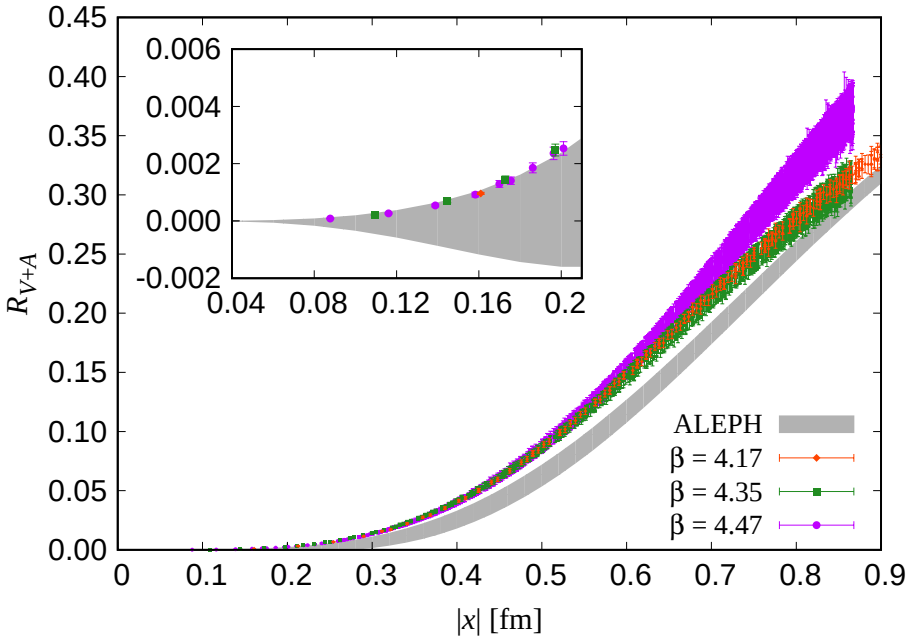

FIG. 11. Same as Figure 10 but calculated on the ensembles at different lattice cutoffs and a matched pion mass $M_\pi \simeq 300$ MeV.

three different β's, there is no significant dependence on the lattice spacing at short distances ($\lesssim 0.5$ fm) unlike the case of the $V+A$ channel. One possible reason for this is that the discretization effect on correlators at short distances is mostly perturbative and cancel in the $V-A$ channel.

We extrapolate $R_{V-A}(x)$ to the physical point in the same manner as for the $V+A$ channel. The result is shown in Figure 12. The consistency between the lattice result and the experiment can be seen in the region $|x| > 0.2$ fm. The extrapolation formula works at $|x| \simeq 0.2$ fm as the fit result of d_i and χ^2/dof indicates (Figures 13 and 14). Unlike the case of the $V+A$ channel, d_i does not vary rapidly and χ^2/dof remains $O(1)$ even at $|x| \simeq 0.2$ fm. At shorter distances, there are few lattice points in a bin B_i and the average of $|x|$ over lattice points in the bin could significantly deviate from the center x_i of the bin depending on a. This may lead to another source of a-dependence of $\overline{R}_{V-A}(a, M_\pi, x_i)$, which may not be taken into account by our fit procedure. Although we do not extrapolate the lattice data in $|x| < 0.2$ fm for this reason, Figures 10 and 11 indicate that the lattice data agree with the phenomenological curve even in the asymptotically small $|x|$ region.

Figure 12 also shows the predictions of OPE including up to dimension-4 (dotted curve)

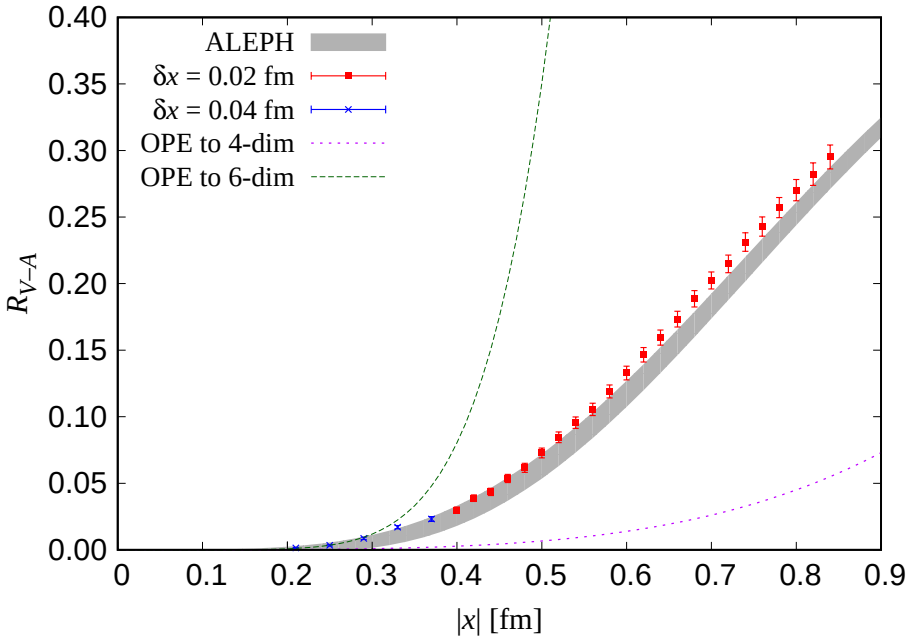

FIG. 12. Lattice result for R_{V-A} after the chiral and continuum extrapolations. Data in each bin are extrapolated assuming (18). Bin size is larger in the short-distance region $|x| \lesssim 0.4$ fm (blue crosses) than others (red squares) as the number of lattice points are fewer. The experimental result (band) and the predictions of OPE including up to dimension-4 (dotted curve) and dimension-6 (dashed curve) operators are also plotted.

and dimension-6 (dashed curve) operators. The OPE $R^{\rm OPE}_{V-A}(x)$ of the $V-A$ channel is written as

$$R^{\rm OPE}_{V-A}(x) = -\frac{\pi^2}{3} m_q \langle \bar{q}q \rangle x^4 + \frac{\alpha_s \pi^3}{9} \langle \bar{q}q \rangle^2 \ln(\mu_0 x)^2 x^6 - \frac{f_\pi^2 m_\pi^3 \pi^2}{48} |x|^5 K_1(m_\pi |x|) + O(m_q^2). \quad (19)$$

Here, only the leading order of the strong coupling constant α_s is shown for the first and second terms. The first term is calculated by the Fourier transform of the OPE in the momentum space given in [31]. The second term is estimated using the vacuum saturation approximation with $\langle \bar{q}q \rangle^2$ [39]. Before the normalization of (13), this term is logarithmic in x with an unknown parameter μ_0 as a result of the Fourier transform $Q^{-4} \to -\frac{1}{16\pi^2} \ln(\mu_0 x)^2$. Since the first two terms on the right hand side of (19) correspond to the OPE including the longitudinal component of the axial-vector correlators, we subtract the contribution of the pion pole by the third term. In the evaluation of $R^{\rm OPE}_{V-A}(x)$ shown in Figure 12, we set nominal values $f_\pi = 130$ MeV, $m_\pi = 140$ MeV, and the scheme-dependent parameters at

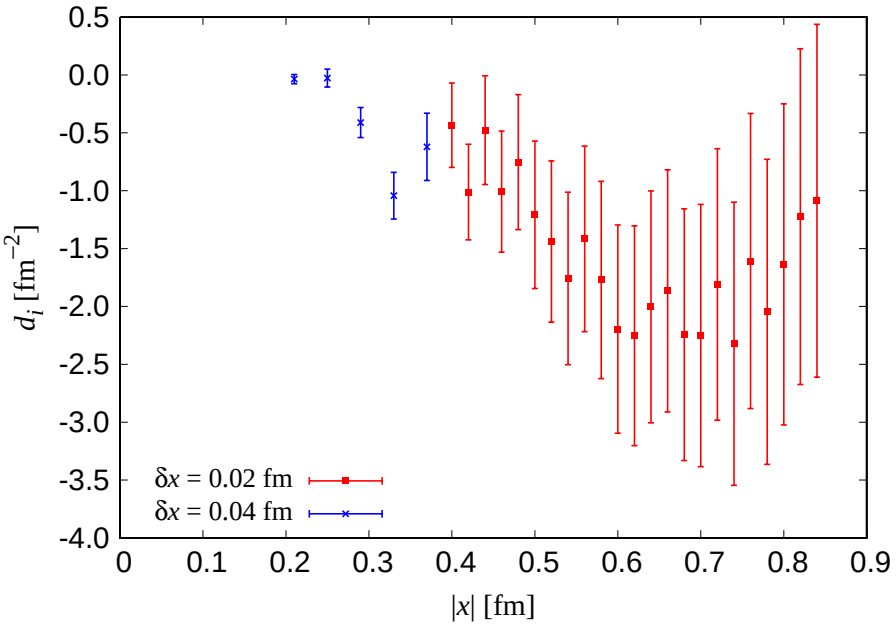

FIG. 13. Same as Figure 8 but the result for the $V - A$ channel.

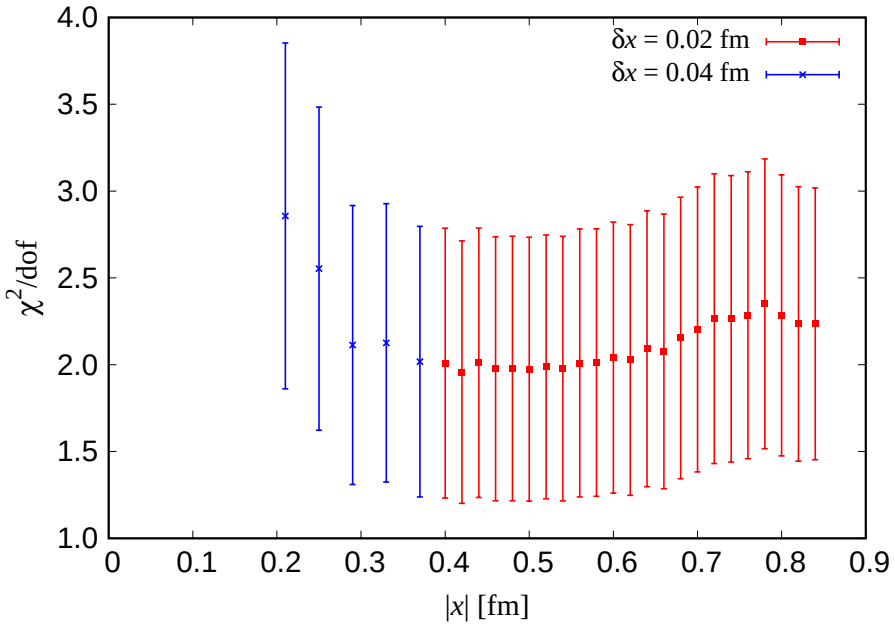

FIG. 14. Same as Figure 9 but the result for the $V - A$ channel.

2 GeV in the $\overline{\rm MS}$ scheme, $\alpha_s = 0.3$, $m_q = 3.4$ MeV, $\langle\bar{q}q\rangle = -(270\ \text{MeV})^3$, and we also set $\mu_0 = 2$ GeV as a typical value. The result of the truncation at dimension-4 deviates from the lattice result already at 0.3 fm. Including the dimension-6 operators, it still disagrees with the lattice result in the region $|x| > 0.3$ fm.

This analysis demonstrates the limitation of the operator expansion quantitatively. The distance scale where OPE can be safely used depend on the channel, and in the $V - A$ channel it is only $\lesssim 0.3$ fm.

C. Chiral condensate

Here, we show our analysis to extract the chiral condensate through the PCAC relation. The basic recipe valid in the continuum theory is explained in Section II B.

On the lattice, some modifications to (12) are needed. The violation of the current conservation induces substantial discretization effects from the derivative term. Such discretization effects can be largely eliminated by subtracting the vector counterpart, which vanishes in the continuum theory.

We analyze

$$\Sigma^{V/A}_{m_q}(x) = -\frac{\pi^2}{2(m_q + m_{res})} x^2 \sum_{\mu,\nu} x_\nu \nabla_\mu \Pi^{\infty}_{V/A,\mu\nu}(x), \tag{20}$$

where the derivative ∇_μ on the lattice is defined as

$$\nabla_\mu f(x) = \frac{f(x + a\hat{\mu}) - f(x - a\hat{\mu})}{2a}, \tag{21}$$

with $\hat{\mu}$ being the unit vector along the μ-direction. The residual mass m_{res} is added to the quark mass to take account of the violation of the Ginsparg-Wilson relation due to finite L_s.

In (20), we use the correlators $\Pi^{\infty}_{V/A,\mu\nu}(x)$ after subtracting the finite volume effect. Here, we assume that there is no significant finite volume effect for the vector channel, $\Pi^{\infty}_{V,\mu\nu}(x) = \Pi_{V,\mu\nu}(x)$, which is justified because the single pion does not propagate in this channel. The finite volume effect on the axial-vector channel is estimated as the wrap-around effect of the pion as in the previous subsection. The asymptotic form of $\sum_{\mu,\nu} x_\nu \nabla_\mu \Pi^{\infty}_{\rm A,\mu\nu}(x)$ at long distances is given by

$$\sum_{\mu,\nu} x_\nu \nabla_\mu \Pi^{\infty}_{A,\mu\nu}(x) \to \frac{M_\pi^2 z_0}{2\pi^2} \sum_{\mu} x_\mu \partial_\mu \frac{K_1(M_\pi|x|)}{|x|}, \tag{22}$$

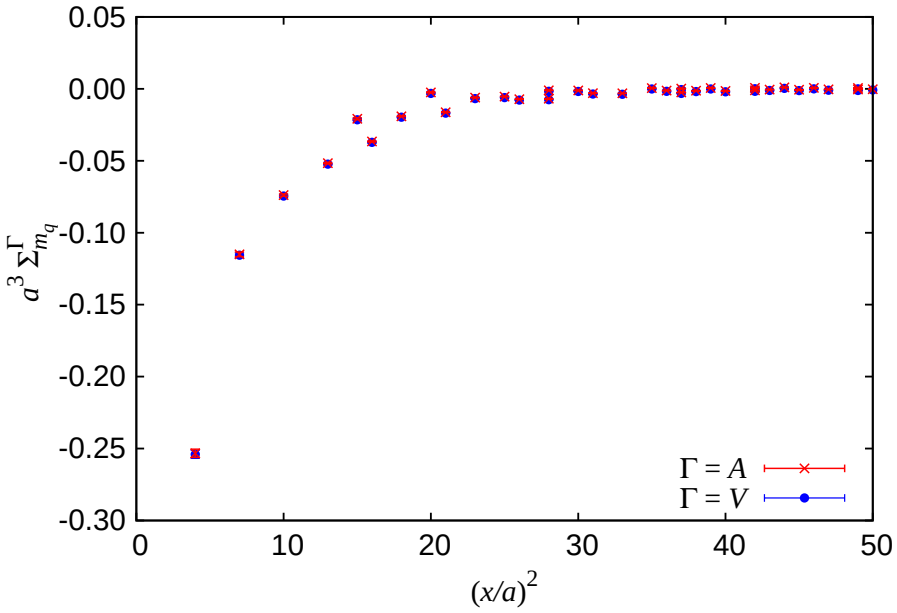

FIG. 15. $\Sigma^{V/A}_{m_q}$ as functions of $(x/a)^2$ calculated on the ensemble at $\beta = 4.35$ and $(am_q, am_s) = (0.0042, 0.0180)$.

where z_0 and M_π may be extracted from the zero-momentum correlator, $\int \mathrm{d}^3x\, \Pi_{A,44}(\vec{x}, t) \to z_0 \mathrm{e}^{-M_\pi t}$. We can thus subtract the finite volume effect from the lattice data by

$$\sum_{\mu,\nu} x_\nu \nabla_\mu \Pi^\infty_{A,\mu\nu}(x) = \sum_{\mu,\nu} x_\nu \nabla_\mu \Pi_{A,\mu\nu}(x) - \frac{M_\pi^2 z_0}{2\pi^2} \sum_{\mu,x_0} x_\mu \partial_\mu \frac{K_1(M_\pi|x - x_0|)}{|x - x_0|}, \tag{23}$$

where the sum over x_0 runs over

$$x_0 \in \{(\pm L, 0, 0, 0), (0, \pm L, 0, 0), (0, 0, \pm L, 0), (0, 0, 0, \pm T), (\pm L, \pm L, 0, 0), \ldots\}. \tag{24}$$

Figure 15 shows the lattice result for $\Sigma^{V/A}_{m_q}(x)$ calculated on one of the ensembles. In the continuum theory, the axial-vector channel $\Sigma^A_{m_q}(x)$ is equal to the chiral condensate up to the correction of $O(m_q)$, as shown in (12), and the vector channel is identically zero. Figure 15 indicates that the axial-vector channel calculated on the lattice almost coincides with the vector channel and non-zero, because of the non-conserving (axial-)vector currents. In other words, the axial-vector channel is largely contaminated by the discretization effect, but by the same amount that the vector channel is. The precise chiral symmetry realized by Möbius domain-wall fermion is the source of this coincidence.

Therefore, we may cancel the bulk of the discretization effects by analyzing

$$\Sigma_{m_q}(x) = \Sigma^A_{m_q}(x) - \Sigma^V_{m_q}(x), \tag{25}$$

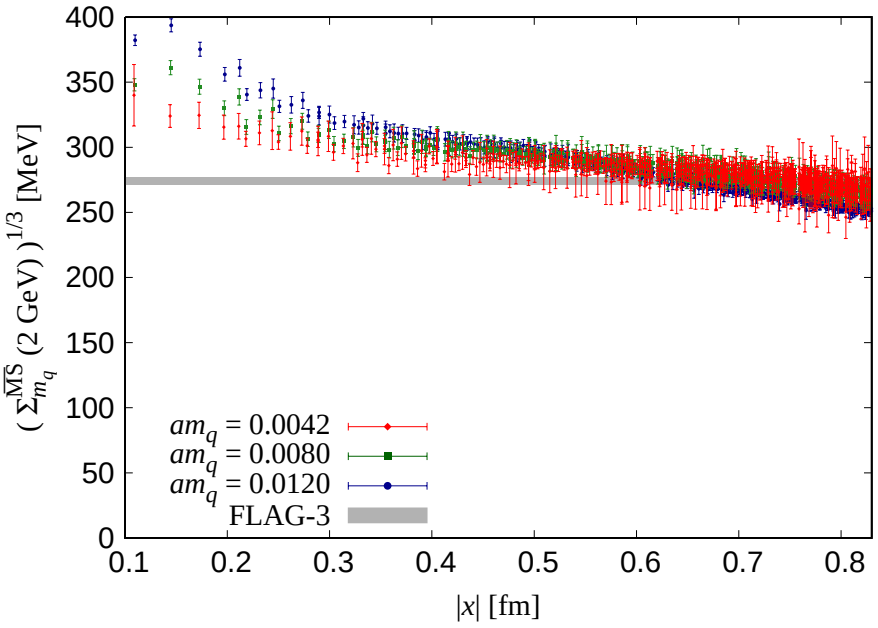

FIG. 16. $(\Sigma^{\overline{\rm MS}}_{m_q}(2\ {\rm GeV}))^{1/3}$ calculated on the ensembles at $\beta = 4.35$, $am_s = 0.0180$ and at three input light quark masses $am_q = 0.0042$ (diamonds), 0.080 (squares) and 0.0120 (circles). The gray band shows the FLAG average $(\Sigma^{\overline{\rm MS}}(2\ {\rm GeV}))^{1/3} = 274(3)$ MeV.

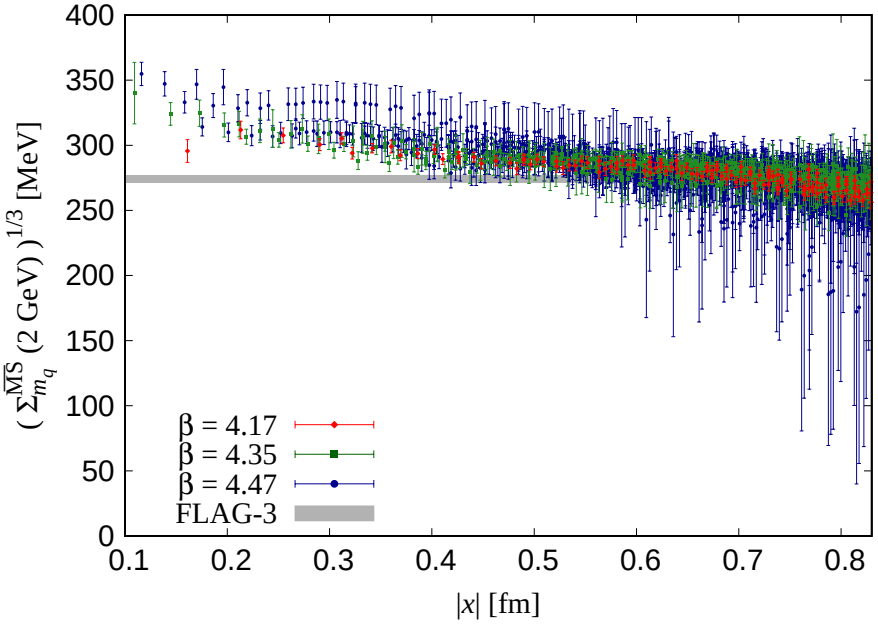

FIG. 17. Same as Figure 16 but calculated on the ensembles at different lattice cutoffs and a matched pion mass $M_\pi \simeq 300$ MeV.

which reduces to $\Sigma^A_{m_q}(x)$ in the continuum theory. Figure 16 shows the cubic root of $\Sigma_{m_q}(x)$ calculated at three different masses and same β. The renormalization is done multiplicatively at 2 GeV to the $\overline{\rm MS}$ scheme,

$$\Sigma^{\overline{\rm MS}}_{m_q}(2\ {\rm GeV}; x) = Z_V^{\overline{\rm MS}}(a)^2 Z_S^{\overline{\rm MS}}(2\ {\rm GeV}; a)\Sigma_{m_q}(x) \tag{26}$$

with the renormalization factors $Z_V^{\overline{\rm MS}}(a)$ and $Z_S^{\overline{\rm MS}}(2\ {\rm GeV}; a)$ determined in the previous work [22]. The gray band represents the FLAG average [40] of the chiral condensate $(\Sigma^{\overline{\rm MS}}(2\ {\rm GeV}))^{1/3} = 274{\pm}3$ MeV at $n_f = 2+1$.

In Figure 16, the results at smaller masses are closer to the FLAG average. This agrees with the theoretical expectation discussed in Section II B that the chiral condensate $\Sigma^{\overline{\rm MS}}(2\ {\rm GeV})$ is obtained in the chiral limit of $\Sigma^{\overline{\rm MS}}_{m_q}(2\ {\rm GeV}; x)$. Figure 17 shows the results at three different lattice spacings with a matched pion mass $M_\pi \simeq 300$ MeV. Like the case for $R_{V-A}(x)$, there is no significant dependence on the lattice spacing.

We extrapolate these results to the chiral and the continuum limits as follows. The average $\overline{\Sigma}^{\overline{\rm MS}}_{m_q}(2\ {\rm GeV}; a, M_\pi, x_i)$ of $\Sigma^{\overline{\rm MS}}_{m_q}(2\ {\rm GeV}; x)$ over lattice points in each bin is defined similarly to $\overline{R}_{V\pm A}(a, M_\pi, x_i)$ in the previous subsections. Unlike the case for $R_{V\pm A}(x)$, the x-dependence of $\Sigma_{m_q}(x)$ is limited to $O(M_\pi^2)$ or $O(a^2)$, and the result of the extrapolation of $\Sigma_{m_q}(x)$ must be independent of x. We therefore perform a simultaneous fit for all bins using the fit function

$$\left(\overline{\Sigma}^{\overline{\rm MS}}_{m_q}(2\ {\rm GeV}; a, M_\pi, x_i)\right)^{1/3} = \left(\Sigma^{\overline{\rm MS}}(2\ {\rm GeV})\right)^{1/3} + c_i M_\pi^2 + d_i a^2, \quad i = 1, 2, \ldots, N, \tag{27}$$

with $2N+1$ parameters $c_1, c_2, \ldots, c_N, d_1, d_2, \ldots, d_N$ and $\left(\Sigma^{\overline{\rm MS}}(2\ {\rm GeV})\right)^{1/3}$.

At short distances, the continuum extrapolation may be contaminated because there are few data points in a bin. At long distances, on the other hand, the extrapolation by the fit function (27) may not be appropriate since the mass dependence of $\Sigma_{m_q}(x)$ may be complicated as described in (22). We extrapolate lattice data at middle distances where the dependences on the pion mass and lattice spacing would be well under control by the fit function (27).

Table II summarizes the results at several fit ranges and widths of bins. The dependence on δx is sufficiently small compared to the statistical error. On the other hand, the dependence on the fit range is larger than the statistical error. Including this uncertainty in the estimate of the systematic error, we determine the chiral condensate as

$$\left(\Sigma^{\overline{\rm MS}}(2\ {\rm GeV})\right)^{1/3} = 284.9 \pm 4.0_{\rm stat} \pm 8.8_{\rm sys}\ {\rm MeV}. \tag{28}$$

TABLE II. Chiral condensate extracted from the global fit using (27) at various fit ranges and bin widths.

$x_1 - \delta x/2$ [fm]	$x_N + \delta x/2$ [fm]	δx [fm]	N	$\Sigma^{\overline{\rm MS}}(2\ {\rm GeV})^{1/3}$ [MeV]
0.23	0.83	0.02	30	284.3(4.0)
0.23	0.83	0.04	15	285.2(4.0)
0.23	0.83	0.06	10	284.5(4.0)
0.23	0.83	0.10	6	285.7(4.0)
0.23	0.43	0.04	5	293.7(5.4)
0.31	0.51	0.04	5	290.7(5.0)
0.39	0.59	0.04	5	288.9(4.6)
0.47	0.67	0.04	5	285.5(4.4)
0.55	0.75	0.04	5	280.8(4.0)
0.63	0.83	0.04	5	276.2(3.8)

Here, the central value and the statistical error are estimated by an average of the four results for the fit range 0.23–0.83 fm with various widths δx, while the systematic error is estimated as the maximum difference between the central value and the results at various fit ranges. This result agrees well with the result obtained from the Dirac spectrum on the same set of lattice ensembles, 270.0(4.9) MeV [20].

V. CONCLUSION

We have discussed the vector and axial-vector current correlators in the distances between the perturbative and non-perturbative regimes. In this intermediate region, neither the perturbative approaches nor low-energy effective theories are fully applicable. Lattice calculation can be used to analyze such theoretically difficult physical regions, provided that the systematic errors are reduced properly estimated. In this work we have demonstrated that the lattice calculation successfully reproduces the experimentally observed spectral functions in QCD. The τ decay experiment by ALEPH played a crucial role as it provides the data for both the vector and axial-vector channels. The $V+A$ channel is useful to mainly

test the perturbation theory, while the $V - A$ is sensitive to the non-perturbative aspects of QCD. If fact, the chiral condensate, the order parameter of chiral symmetry breaking, can be precisely extracted from this analysis.

The consistency between the lattice calculation and the experimental data seen in this work adds another support for the validity of QCD in the distance region where excited states contribute significantly. The lattice calculation of the current correlators can also identify the region where the correlators are well explained by OPE, which is the main theoretical tool in phenomenological analyses.

The method applied in this work to extract the chiral condensate needs a differential of the axial-vector correlator on the lattice. The substantial discretization error from the differential is dramatically reduced by subtracting the counterpart of the vector channel. The fact that thus obtained chiral condensate agrees with that based on the Banks-Casher relation gives another confidence about our description of the symmetry broken QCD vacuum.

Lattice calculation of current correlators at finer lattices, which will become available in the near future, would be very interesting as it may give further information in the perturbative regime. It will provide us with a stringent test of the perturbative expansion in QCD, which is now available to $O(\alpha_s^4)$ for the vacuum polarization function. At the same time, it would be a sensitive probe to determine the strong coupling constant.

While this work focused on the vector and axial-vector channels, the scalar and pseudoscalar correlators may reflect a different aspect of QCD. The perturbative region for these correlators is much shorter than that of the vector and axial-vector channels because they are directly affected by the instanton interactions [41]. Lattice calculation of the scalar and pseudoscalar correlators may give new insights to understand such effects.

ACKNOWLEDGMENTS

Numerical simulations are performed on Hitachi SR16000 and IBM Blue Gene/Q at KEK under a support of its Large Scale Simulation Program (No. 15/16-09, 16/17-14). We thank P. Boyle for providing the highly optimized code for Blue Gene/Q. This work is supported in part by the Grant-in-Aid of the Japanese Ministry of Education (No. 25800147, 26247043,

26400259) and the Post-K supercomputer project through JICFuS.

---

[1] E. V. Shuryak, *Rev. Mod. Phys.* **65** (1993) 1–46.

[2] T. Schaefer and E. V. Shuryak, *Phys. Rev. Lett.* **86** (2001) 3973–3976, arXiv:hep-ph/0010116 [hep-ph].

[3] M. C. Chu, J. M. Grandy, S. Huang, and J. W. Negele, *Phys. Rev.* **D48** (1993) 3340–3353, arXiv:hep-lat/9306002 [hep-lat].

[4] **UKQCD** Collaboration, S. J. Hands, P. W. Stephenson, and A. McKerrell, *Phys. Rev.* **D51** (1995) 6394–6402, arXiv:hep-lat/9412065 [hep-lat].

[5] T. A. DeGrand, *Phys. Rev.* **D64** (2001) 094508, arXiv:hep-lat/0106001 [hep-lat].

[6] M. Davier, A. Hocker, B. Malaescu, C.-Z. Yuan, and Z. Zhang, *Eur. Phys. J.* **C74** no. 3, (2014) 2803, arXiv:1312.1501 [hep-ex].

[7] P. A. Baikov, K. G. Chetyrkin, and J. H. Kuhn, *Phys. Rev. Lett.* **101** (2008) 012002, arXiv:0801.1821 [hep-ph].

[8] P. A. Baikov, K. G. Chetyrkin, and J. H. Kuhn, *Nucl. Phys. Proc. Suppl.* **189** (2009) 49–53, arXiv:0906.2987 [hep-ph].

[9] M. A. Shifman, in *Workshop on Continuous Advances in QCD Minneapolis, Minnesota, February 18-20, 1994*. 1994. arXiv:hep-ph/9405246 [hep-ph].

[10] B. Blok, M. A. Shifman, and D.-X. Zhang, *Phys. Rev.* **D57** (1998) 2691–2700, arXiv:hep-ph/9709333 [hep-ph]. [Erratum: Phys. Rev.D59,019901(1999)].

[11] M. A. Shifman, in *Proceedings, 8th International Symposium on Heavy Flavor Physics (Heavy Flavors 8)*, p. hf8/013. 2000. arXiv:hep-ph/0009131 [hep-ph]. [,hf8/013(2000)].

[12] I. I. Y. Bigi and N. Uraltsev, *Int. J. Mod. Phys.* **A16** (2001) 5201–5248, arXiv:hep-ph/0106346 [hep-ph].

[13] O. Cata, M. Golterman, and S. Peris, *Phys. Rev.* **D79** (2009) 053002, arXiv:0812.2285 [hep-ph].

[14] D. Boito, M. Golterman, M. Jamin, A. Mahdavi, K. Maltman, J. Osborne, and S. Peris, *Phys. Rev.* **D85** (2012) 093015, arXiv:1203.3146 [hep-ph].

[15] R. C. Brower, H. Neff, and K. Orginos, *Nucl. Phys. Proc. Suppl.* **140** (2005) 686–688, arXiv:hep-lat/0409118 [hep-lat]. [,686(2004)].

[16] R. C. Brower, H. Neff, and K. Orginos, arXiv:1206.5214 [hep-lat].

[17] B. Fahy, G. Cossu, S. Hashimoto, T. Kaneko, J. Noaki, and M. Tomii, in *Proceedings, 33rd International Symposium on Lattice Field Theory (Lattice 2015)*. 2015. arXiv:1512.08599 [hep-lat].

[18] **JLQCD** Collaboration, T. Kaneko, B. Fahy, H. Fukaya, and S. Hashimoto, in *Proceedings, 34th International Symposium on Lattice Field Theory (Lattice 2016): Southampton, UK, July 24-30, 2016*. 2017. arXiv:1701.00942 [hep-lat]. http://inspirehep.net/record/1507795/files/arXiv:1701.00942.pdf.

[19] K. Nakayama, B. Fahy, and S. Hashimoto, *Phys. Rev.* **D94** no. 5, (2016) 054507, arXiv:1606.01002 [hep-lat].

[20] G. Cossu, H. Fukaya, S. Hashimoto, T. Kaneko, and J.-I. Noaki, *PTEP* **2016** no. 9, (2016) 093B06, arXiv:1607.01099 [hep-lat].

[21] **JLQCD** Collaboration, H. Fukaya, S. Aoki, G. Cossu, S. Hashimoto, T. Kaneko, and J. Noaki, *Phys. Rev.* **D92** no. 11, (2015) 111501, arXiv:1509.00944 [hep-lat].

[22] **JLQCD** Collaboration, M. Tomii, G. Cossu, B. Fahy, H. Fukaya, S. Hashimoto, T. Kaneko, and J. Noaki, *Phys. Rev.* **D94** no. 5, (2016) 054504, arXiv:1604.08702 [hep-lat].

[23] G. Martinelli, G. C. Rossi, C. T. Sachrajda, S. R. Sharpe, M. Talevi, and M. Testa, *Phys. Lett.* **B411** (1997) 141–151, arXiv:hep-lat/9705018 [hep-lat].

[24] V. Gimenez, L. Giusti, S. Guerriero, V. Lubicz, G. Martinelli, S. Petrarca, J. Reyes, B. Taglienti, and E. Trevigne, *Phys. Lett.* **B598** (2004) 227–236, arXiv:hep-lat/0406019 [hep-lat].

[25] K. Cichy, K. Jansen, and P. Korcyl, *Nucl. Phys.* **B865** (2012) 268–290, arXiv:1207.0628 [hep-lat].

[26] K. G. Chetyrkin and A. Maier, *Nucl. Phys.* **B844** (2011) 266–288, arXiv:1010.1145 [hep-ph].

[27] C. Becchi, S. Narison, E. de Rafael, and F. J. Yndurain, *Z. Phys.* **C8** (1981) 335.

[28] **ALEPH** Collaboration, R. Barate *et al.*, *Z. Phys.* **C76** (1997) 15–33.

[29] **ALEPH** Collaboration, R. Barate *et al.*, *Eur. Phys. J.* **C4** (1998) 409–431.

[30] **ALEPH** Collaboration, S. Schael *et al.*, *Phys. Rept.* **421** (2005) 191–284, arXiv:hep-ex/0506072 [hep-ex].

[31] M. A. Shifman, A. I. Vainshtein, and V. I. Zakharov, *Nucl. Phys.* **B147** (1979) 385–447.

[32] M. Jamin and M. Munz, *Z. Phys.* **C60** (1993) 569–578, arXiv:hep-ph/9208201 [hep-ph].

[33] M. Luscher and P. Weisz, "On-Shell Improved Lattice Gauge Theories," *Commun. Math. Phys.* **97** (1985) 59. [Erratum: Commun. Math. Phys.98,433(1985)].

[34] C. Morningstar and M. J. Peardon, *Phys. Rev.* **D69** (2004) 054501, arXiv:hep-lat/0311018 [hep-lat].

[35] M. Luscher, *JHEP* **08** (2010) 071, arXiv:1006.4518 [hep-lat]. [Erratum: JHEP03,092(2014)].

[36] S. Borsanyi *et al.*, *JHEP* **09** (2012) 010, arXiv:1203.4469 [hep-lat].

[37] G. Cossu, J. Noaki, S. Hashimoto, T. Kaneko, H. Fukaya, P. A. Boyle, and J. Doi, in *Proceedings, 31st International Symposium on Lattice Field Theory (Lattice 2013)*. 2013. arXiv:1311.0084 [hep-lat].

[38] G. P. Lepage and P. B. Mackenzie, *Phys. Rev.* **D48** (1993) 2250–2264, arXiv:hep-lat/9209022 [hep-lat].

[39] S. Narison and V. I. Zakharov, *Phys. Lett.* **B522** (2001) 266–272, arXiv:hep-ph/0110141 [hep-ph].

[40] S. Aoki *et al.*, arXiv:1607.00299 [hep-lat].

[41] V. A. Novikov, M. A. Shifman, A. I. Vainshtein, and V. I. Zakharov, *Nucl. Phys.* **B191** (1981) 301.